Large displacement FEM modelling of the cone penetration test (CPT) in normally consolidated sand

Endra Susila and Roman D. Hryciw*,†

Department of Civil and Environmental Engineering, The University of Michigan, Ann Arbor, MI-48109-2125, USA

SUMMARY

A new finite element model based on a large strain formulation has been developed to study cone penetration in normally consolidated sand. An auto-adaptive remeshing technique was utilized for handling the very large distortion of sand surrounding the cone tip. A frictional contact interface utilizing Mohr–Coulomb's theory was chosen to represent interactions between the surface of the cone and sand. To model the sand behaviour, the non-associated Drucker–Prager constitutive model was selected. ABAQUS, a commercial finite element software package, was used to implement the model. The explicit solution algorithm was chosen due to its effectiveness for complicated contact problems. Analysis results proved that the model successfully captured the cone penetration behavior in sand. In addition, a chart to predict internal friction angles based on cone tip resistance for different vertical effective stresses was provided. This paper also shows a typical distribution of sleeve resistance, tip resistance—penetration relationship, and typical contours of vertical, horizontal, and shear stresses in normally consolidated sand. Finally, a non-uniform resistance was found along the length of the friction sleeve. Copyright © 2003 John Wiley & Sons, Ltd.

KEY WORDS: cone penetration; sand; FEM modelling; adaptive remeshing

1. INTRODUCTION

Various analytical methods have been used to study cone penetration in sand, including: bearing capacity theories by limit plasticity [1–4], cavity expansion theories [5–7] and the strain path method [8]. Laboratory studies using calibration chamber tests have also been performed to study cone penetration [9–12]. Numerically, Kiousis *et al*. [13], Van Den Berg *et al*. [14] and Abu-Farsakh *et al*. [15] used the finite element method to study cone penetration in soils.

Developments in computer technology that have led to higher computational speeds and greater memory have reduced the cost of complicated analysis. The finite element method can easily implement any type of constitutive model, solve problems with difficult geometries, and provide solutions with a high degree of accuracy. For cone penetration modelling, the finite element method has many advantages: soil stiffness and compressibility can easily be modelled,

*Correspondence to: Roman D. Hryciw, Department of Civil and Environmental Engineering, The University of Michigan, 2366 GG Brown Building, Ann Arbor, MI-48109-2125, USA
†E-mail: romanh@umich.edu

initial stresses may be prescribed, increases in stress during the penetration can accurately be determined, failure modes do not have to be assumed, both equilibrium equations and yield criterion are satisfied, and various constitutive models can be utilized.

However, cone penetration modelling by finite elements has hitherto been plagued by very large mesh distortion in zones of high strain concentration around the cone tip. When penetration distances are large, mesh distortion leads to a severe loss of accuracy, a reduction in the stable time increment and numerical divergence. Furthermore, the inherent CPT geometry and the boundary condition along the center line below the CPT add to the modelling difficulty.

Kiousis et al. [13] presented a large strain formulation and used the strategy of changing the boundary conditions around the cone tip with each penetration step. However, since boundary nodes have to be relocated, the soil displacement pattern does not develop naturally. Van den Berg [16] pointed out that the changing boundaries also complicate the modelling of cone penetration when a frictional interface is implemented.

Today's finite element technology offers two techniques for solving very large mesh distortions such as found in problems of extrusion, forging, rolling, metal forming and cone penetration. The first technique is called the Arbitrary Lagrangian Eulerian (ALE) formulation while the second approach uses adaptive remeshing strategies based on a Lagrangian formulation [17]. In the first technique, the evolution of the mesh and material particles are uncoupled and the mesh evolution is constrained so that excessive mesh distortion is avoided [17]. Van Den Berg et al. [14] used this method to study cone penetration. The second approach uses a Lagrangian formulation and when the mesh distorts, it is 'adapted' using a special remeshing technique [17]. The remeshing technique that is used in this analysis is the ALE technique. The model involves: (1) re-discretizing the deformed boundaries and generation of a new mesh, and (2) transfer of the field variables that define the mechanical state to the new mesh [17]. Hamel et al. [17] stated their belief that the adaptive remeshing technique has advantages for problems which are very dependent on the geometrical and material parameters and the complexities of the contact interface. However, comparison has not yet been made to determine which technique would be more suitable for cone penetration simulation.

In this paper, the auto-adaptive remeshing technique is used because it maintains a high-quality mesh throughout an analysis. The commercial finite element software ABAQUS was utilized to employ the technique. Frictional contact, instead of smooth interfaces, is used to model the interaction between the cone and soils. This decision was prompted by studies [3, 4, 15] which showed that the interface friction had a significant effect on cone resistance. Finally, instead of a rigid body assumption, the cone steel is modelled by elastic elements so that the cone may deform and thus, sleeve friction can be evaluated.

An explicit iteration technique is used based on the studies by Rebelo et al. [18], Sun et al. [19] and Hibbitt et al. [20] which concluded that for very complex analyses with large domains and very fine meshes, the explicit techniques are more efficient than implicit ones. The reason is that the analysis cost (run time) of the explicit procedure increases in direct proportion to the size of the mesh. By contrast, the analysis cost for the implicit procedure increases with the square of the wave-front times the number of degrees of freedom [18]. The effectiveness of the explicit solution for complicated problems allows us to develop a very fine mesh, especially in the area which is in contact with the cone elements. To assure accurate solutions, the ratio of soil element size to cone radius was kept small. Finally, infinite elements were prescribed at the base and perimeter of the model to minimize the effects of boundaries.

The goal of this research is to develop a rigorous method to simulate cone penetration into sands. If proven successful, the method could be utilized to study geologic situations that cannot be solved using closed-form methods. These include stratified soils and complex stress states. This paper demonstrates the proposed method by parametrically studying the effects of the angle of internal friction (ϕ) of normally consolidated sands and the initial effective overburden stress (σ'_{vo}) on cone tip resistance (q_c). A chart correlating q_c to ϕ as a function of σ'_{vo} is developed. The chart is compared with results of earlier studies. This paper will also present typical q_c vs penetration data, a typical sleeve friction vs penetration plot, the distribution of sleeve friction along a cone shaft and typical soil stress contours.

2. EXPLICIT SOLUTIONS FOR QUASI-STATIC ANALYSIS

The explicit technique was developed to solve the inefficiency of the implicit solution for complex problems. Rebelo *et al.* [18] and Hibbit *et al.* [20] have utilized explicit techniques to simulate quasi-static problems in the metal forming processes and compared the results with implicit technique solutions. Sun *et al.* [19] also performed a study to compare implicit and explicit techniques for dynamic problems. The study by Rebelo *et al.* [18] concludes that the explicit algorithm is better suited to complex problems dominated by highly discontinuous non-linearity. In the implicit solution, the cost of analysis increases much faster than the size of the model due to the increasing wave-front size, the number of increments, and iterations [18]. For very complex problems, in which the time increment continuously decreases, the computational cost of the implicit technique will dramatically increase and can cause divergence [19]. By contrast, the size of the time increment in the explicit technique is only dependent on the element dimensions and material properties, not on the complexity of the analysis. The solution time in the explicit technique is therefore generally not affected by complex contact conditions [21].

The explicit integration rule together with the use of diagonal or lumped element mass matrices are used in the explicit dynamic analysis procedure [21]. The equations are integrated using the following explicit central difference integration rule:

$$\dot{u}_{(i+1/2)} = \dot{u}_{(i-1/2)} + \frac{\Delta t_{(i+1)} + \Delta t_{(i)}}{2} \ddot{u}_{(i)}$$

$$u_{(i+1)} = u_{(i)} + \Delta t_{(i+1)} \dot{u}_{(i+1/2)}$$

where i is the increment number, u the displacement, and Δt the time increment.

The key to the computational efficiency of the explicit procedure is the use of diagonal mass matrices [21]. The accelerations at the beginning of the increment can be computed by inverting the mass matrix:

$$\ddot{u}_{(i)} = M^{-1} \cdot (F_{(i)} - I_{(i)})$$

Where M is the diagonal lumped mass matrix, F is the applied load vector, and I is the internal force vector.

Conditional stability is a requirement of the explicit technique. It is achieved by assigning the time-step, Δt, to be less than a critical value based on the highest eigenvalue in the

model:

$$\Delta t \leqslant \frac{2}{\omega_{max}}$$

where ω_{max} is the highest eigenvalue in the system.

   Analysis acceleration (using mass/density scaling, load factoring, and speed scaling) was not used to assure a small kinetic energy compared to the strain energy. Using the chosen FE model and given the material properties, it was believed that the analysis was still inexpensive without analysis acceleration. The ratio between the kinetic energy and the strain energy, which in this analysis was on the order of 10^{-3}, assured that the inertia effects would be small.

3. AUTO-ADAPTIVE REMESHING

Auto-adaptive remeshing is utilized to preserve a high quality mesh during penetration of the cone, to maintain calculation accuracy, and to assure converging calculations. Several remeshing techniques have been used, such as h-adaptivity, p-adaptivity, and r-adaptivity [22]. The ALE technique that is used to adapt the mesh in this analysis can be considered as an r-adaptive scheme [23]. The r-adaptivity scheme changes the distorted mesh by relocating nodes without adding or deleting degrees of freedom. Mesh density and mesh gradation from the area closer to the cone to the end boundaries are controlled by creating a high quality mesh at the beginning of the analysis. The mesh gradation is maintained during remeshing throughout the analysis.

   Remeshing involves several steps. First, the element formulations, boundary conditions, external loads, contact conditions, etc. are handled in a manner consistent with a pure Lagrangian analysis. The process then continues by re-discretizing the deformed boundaries and generating the new mesh [21]. ABAQUS requires a small enough geometrical mesh difference between the old mesh and the new mesh to maintain numerical stability. An intermediate mesh is therefore needed if the total accumulated movement of any node in the domain is large compared to the characteristic length of any adjacent element [21].

   Instead of using an error check control, remeshing is performed at a set frequency. Since remeshing frequency is the most significant factor affecting the mesh quality and the computational efficiency, the frequency must be chosen judiciously. Based on the suggestions of Hibbit *et al.* [21], remeshing was performed every 10 increments. A smooth mesh is created by iteratively remeshing the adaptive mesh domain several times. The final step is remapping of variables from the old mesh to the new mesh, which is called an 'advection sweep'.

   The method for relocating nodes is called 'weighted area smoothing'. In this method, each surrounding element pulls the node toward its centre as shown in Figure 1. The movement vector of node M will be the resultant of the summation of vectors v_i times their areas, A_i, normalized by the summation of the areas of all the elements. Node M in Figure 1 will move away from element center c_1 toward element center c_3.

   The advection sweep transfers element and material state variables from the old mesh to the new mesh. The second-order advection method based on the work by Van Leer [25, 26] is chosen for the sweep advection to remap the variables [21]. Using this method, advection is performed by first developing a quadratic interpolation between adjacent elements. Since the elements are the reduced integration elements, the quadratic functions are constructed at the integration
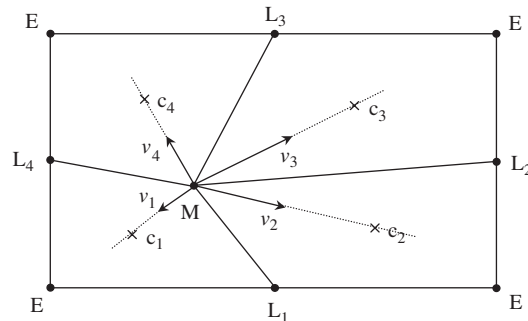
Figure 1. Relocation of a node using weighted area method (after [21, 24]).

points located at the middle of the elements. Quadratic interpolation is then used to develop a trial linear distribution by calculating the slope at the element centers. The final slope for the next calculation is obtained by reducing the trial slope until the value is within the range of the original constant values of the adjacent elements [21]. The slope, a linear distribution, is then used to obtain the new variable for the new mesh.

4. CONTACT INTERFACE

A pure master–slave relationship is used to model contact between two surfaces. In this work, the steel cone was chosen as the master and the soil as the slave. Nodes of the master surface can penetrate the slave surface, but not *vice versa*. It is believed that this algorithm gives a relatively accurate solution for cone penetration. A balanced master–slave model, which completely prohibits penetration, was not chosen to avoid very expensive calculation. Penetration of the master into the slave surface is minimized by refining the mesh of the slave.

The present model uses a kinematic, predictor/corrector contact algorithm as opposed to a penalty method, which has a weaker enforcement of contact constraints. In the kinematic predictor/corrector algorithm, the resisting force is based on the depth of a slave node's penetration, the mass associated with the penetration, and the time increment [21]. The resisting forces of all slave nodes are distributed to the nodes on the master surface. The mass of the slave nodes is also distributed to the master surface nodes. The total inertial mass of the contacting surfaces can be calculated from the additional node mass of the slave and master surfaces [21].

The contact interface is modelled in such a way that it will not transmit contact pressure in either the normal or tangential direction unless the nodes of the slave surface contact the master surface. The magnitude of the transmitted contact pressure is not limited. Transfer of tensile stress is not allowed across the interface. For the tangential direction, the classical isotropic Coulomb friction model without a cap was chosen. The coefficient of interface friction is assumed to be a function of the angle of internal friction [3, 4] and the value is maintained constant throughout an analysis.

For tracking contact nodes, this analysis uses a 'finite sliding algorithm' to ensure correct pairing of nodes and elements of master and slave surfaces. This algorithm can guarantee better quality results compared to a 'small sliding algorithm'. The finite sliding algorithm tracks and

pairs node and element pairs between master and slave surfaces until the calculation stops. By contrast, a small sliding algorithm would have tracked and paired node and element pairs only at the beginning of the first step [21].

5. FINITE ELEMENT MODEL

Figure 2 shows the finite element model for the analysis. Both the soil and the steel cone are modelled using four node axisymmetric elements with one reduced integration point (CAX4R
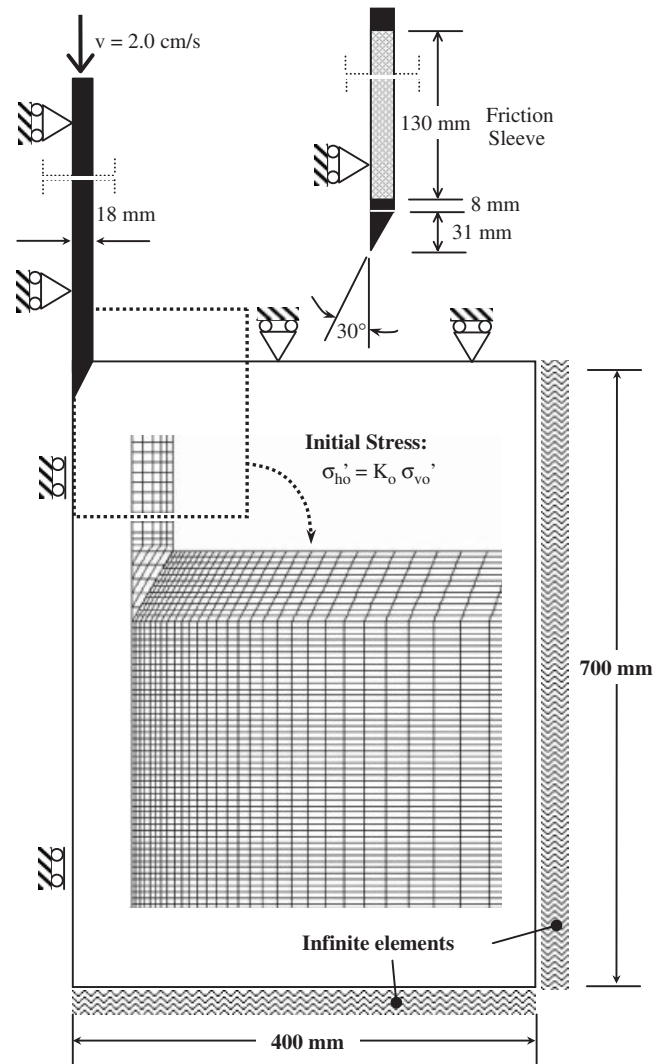

Figure 2. Finite element mesh, geometry, initial positions, and boundary conditions.

ABAQUS element). Several reduced integration three-node elements (CAX3R ABAQUS element) are also used but only in the cone tip. Adaptive remeshing is applied only to soil elements that are close to the cone. To minimize the effects of boundary conditions, 'infinite elements' are utilized at the base and at a radial distance of 400 mm from the cone center line. The infinite elements are only utilized well beyond the area where plastic deformation occurs. This model can be expected to eliminate the effects of boundaries without requiring a prohibitively large model size. Continuous penetration is simulated by imposing a standard CPT penetration rate of 2 cm/s to the top of cone rod.

While Van Den Berg *et al.* [14] placed the cone into a 'pre-bored' hole, in this study the cone is introduced at the top of the soil mesh as shown in Figure 2. The horizontal stress on the cone in a pre-bored model could be significantly underestimated. The top soil elements are restrained from vertical displacement. Therefore, in all simulations, the resistances are only considered after the cone penetrates a sufficient distance such that the effects of the boundary at the top are negligible.

6. PARAMETERS

Coefficient of interface friction between steel and sand. Based on direct shear tests on various surface materials, Durgunoglu and Mitchell [3–4] suggested using $\delta/\phi = 0.50$ for most penetrometers used in practice, where ϕ = peak angle of effective internal friction and δ is the angle of interface friction. In the present studies $\delta/\phi = 0.50$ was used. Table I summarizes the coefficients of friction that were used.

Initial stress. The CPT simulation was performed to a 400 mm depth at three effective vertical stresses, σ'_{vo}. A normally consolidated initial state is represented by the at rest coefficient of lateral pressure $K_o = 1 - \sin\phi$ [27]. Table I summarizes the coefficients of lateral pressure used. Since the 400 mm vertical increment of soil being penetrated is small compared to its simulated depth, a uniform initial state of stress was assumed prior to penetration.

Dilation angle. Dilation angles for the non-associated model were calculated by adopting the 'saw blade' model of dilatancy:

$$\phi = \phi_{cv} + \psi$$

Table I. Coefficient of interface friction between cone and sands

Angle of internal friction (ϕ) (deg)	Coeff. of interface friction, $\mu = \tan\delta$ (where: $\delta = 0.50\ \phi$)	Coefficient of lateral earth pressure at rest, $K_0 = 1 - \sin\phi$
32	0.287	0.470
34	0.306	0.441
36	0.325	0.412
38	0.344	0.384
40	0.364	0.357
42	0.384	0.331

where ϕ is the peak angle of effective internal friction in degrees, ϕ_{cv} the constant volume angle of internal friction in degrees, and ψ the dilation angle.

The empirical 0.8 factor was not applied to ψ as suggested by Bolton's [28] for plane strain problems. The peak angle of internal friction (ϕ) was chosen as the basis for parametric analysis, because it is the fundamental strength parameter used in practical geotechnical design. A constant value of $\phi_{cv} = 33°$ was utilized based on Bolton's [28] observation for silica sands. Ideally, the dilation angle (ψ) should be modelled as a function of soil strain. However, for simplicity, a constant value for ψ was used. The calculated dilation angles in the τ–σ coordinate system are shown in Table II. The dilation angles are then transferred to the p–t coordinate system which will be presented in the next section.

Shear strength and plasticity parameters. The non-associative Drucker–Prager model [29] was implemented in this work. Since ABAQUS [21] requires parameters in the p–t coordinate system, calculations need to be performed to transfer soil parameters from the τ–σ to the p–t coordinate system. The following explanations will summarize References [21, 30] which provide detailed explanation for obtaining parameters for the Drucker–Prager soil model.

Figure 3 shows the yield surface criteria and the hardening rule in the p–t coordinate system. The linear Drucker–Prager criterion can be formulated as:

$$F = t - p \tan \beta - d = 0$$

While the flow potential is expressed as

$$G = t - p \tan \psi^* = 0$$

Table II. Dilation angles in the p–t coordinate system and elastic drained Young's modulus

| Angle of internal friction (ϕ)	σ'_{vo} (MPa)	σ'_{ho} (MPa)	Soil strength parameters				Parameters for Young's modulus				
			ψ (deg)	β (deg)	ψ^* (deg)	K	K_E	n	R_f	E_t (MPa)	v
32	0.05	0.02	0	52.2	0	0.778	380	0.66	0.900	4.4	0.30
	0.16	0.08	0							9.6	
	0.35	0.17	0							16.0	
34	0.05	0.02	1	54.0	2.0	0.778	480	0.64	0.874	5.8	0.30
	0.16	0.07	1							12.2	
	0.35	0.15	1							20.2	
36	0.05	0.02	3	55.6	6.1	0.778	600	0.62	0.825	7.8	0.30
	0.16	0.07	3							16.1	
	0.35	0.14	3							26.1	
38	0.05	0.02	5	57.2	10.2	0.778	750	0.60	0.782	10.4	0.30
	0.16	0.06	5							20.9	
	0.35	0.13	5							33.4	
40	0.05	0.02	7	58.6	14.3	0.778	915	0.58	0.743	13.4	0.30
	0.16	0.06	7							26.3	
	0.35	0.13	7							41.4	
42	0.05	0.02	9	59.9	18.3	0.778	1,110	0.56	0.707	17.0	0.30
	0.16	0.05	9							32.7	
	0.35	0.12	9							50.7	
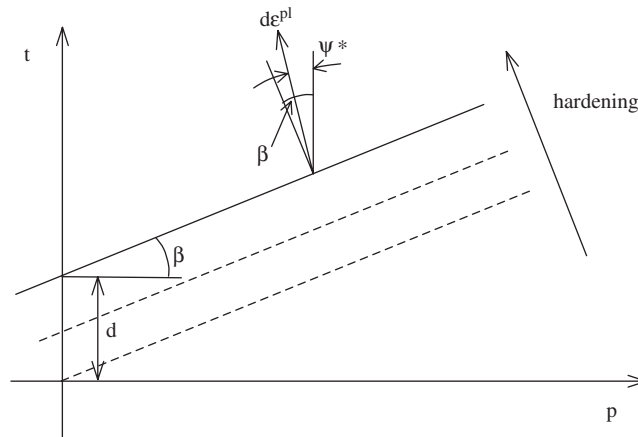
Figure 3. Non-associative Drucker–Prager Model [29, 21].

where

$$t = \frac{1}{2} q \left[1 + \frac{1}{K} - \left(1 - \frac{1}{K} \right) \left(\frac{r}{q} \right)^3 \right]$$

$$p = \frac{1}{3} \text{ trace } \sigma$$

$$q = \sqrt{\frac{3}{2} S : S}$$

where $S = \sigma + pI$ is the deviatoric stress.

$$r = \left(\frac{9}{2} S \cdot S : S \right)^{1/8}$$

β is the angle of the linear yield surface in the p–t stress plane, analogous to, ϕ, d the t-axis intercept in the p–t stress plane, analogous to cohesion, and K the ratio of the yield stress in triaxial extension to yield stress in triaxial compression.

By matching with the Mohr–Coulomb criteria, Chen [30] obtained β using the following equation:

$$\tan \beta = \frac{6 \sin \phi}{3 - \sin \phi}$$

The effective cohesion intercept in the p–t coordinate space, d and K can be calculated as:

$$d = c \frac{6 \cos \phi}{3 - \sin \phi}$$

$$K = \frac{3 - \sin \phi}{3 + \sin \phi}$$

where, c is the effective cohesion intercept in the τ–σ coordinate space.

By analogy to the equation to calculate β from ϕ above, the dilation angle in the p–t coordinate system can be expressed as

$$\tan \psi^* = \frac{6 \sin \psi}{3 - \sin \psi}$$

where, ψ is the dilation angle in the τ–σ coordinate space and ψ^* is the dilation angle in the p–t space.

Table II presents the calculated β, ψ^* and K used in this study. In all cases, $d = c = 0$.

Young's modulus. Duncan and Chang's hyperbolic model [31] was used to calculate the elastic Young's modulus. This elastic modulus is needed below the yield surface. Their formulation can be expressed as follows:

$$E_t = \left[1 - \frac{R_f(1 - \sin \phi)(\sigma_1 - \sigma_3)}{2c \cos \phi + 2\sigma_3 \sin \phi} \right]^2 K_E P_a \left(\frac{\sigma_3}{P_a} \right)^n$$

where E_t is the tangent drained Young's modulus, R_f the failure ratio $R_f = \sigma_f / \sigma_{ult}$, σ_f the stress condition at failure [31], σ_{ult} the asymptotic value of stress [31], K_E the modulus number for primary loading, n the modulus exponent, P_a the atmospheric pressure (100 kPa), σ_1 the major principal stress, and σ_3 the minor principal stress.

R_f was calculated as $0.9(\phi_{cv}/\phi)$ based on the work of Byrne *et al.* [32], where $\phi_{cv} = 33°$ for silica sand.

K_E was chosen as a function of ϕ in accordance with trends observed by Duncan and Chang [31], Duncan *et al.* [33], and Boscardin *et al.* [34] as shown in Figure 4. The parameter n has shown very little correlation to ϕ to previous studies. Fortunately, the results described in this paper were not very sensitive to n, and thus, typical values of $n = 0.56$–0.66 were used. Table II summarizes all of the parameters used in this analysis.
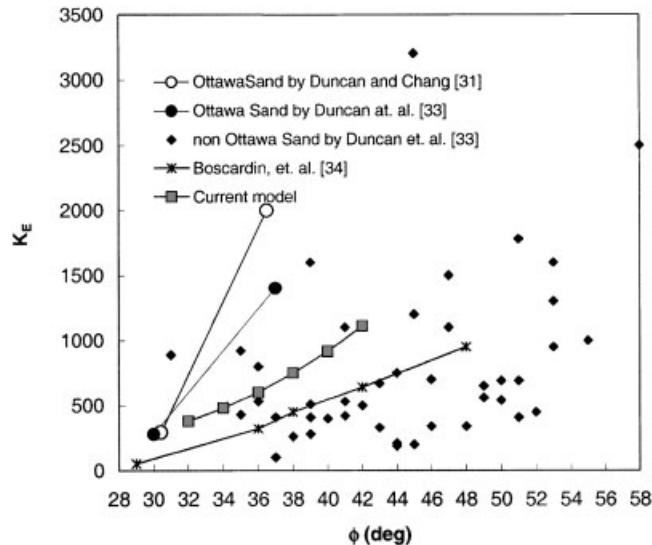

Figure 4. K_E parameter.

7. RESULTS AND DISCUSSION

7.1. Deformed mesh

Figure 5(a) shows a deformed mesh after 20 cm of penetration using a pure Lagrangian method without remeshing. By contrast, Figure 5(b) shows the deformed mesh after a steady cone tip resistance has been reached and after auto-adaptive remeshing. Clearly, the quality of the deformed mesh in Figure 5(b) is better than in Figure 5(a). This confirms the ability of the adaptive remeshing to maintain a high quality mesh during penetration. Figure 5(b) also shows that the chosen adaptive mesh domain was large enough to accomplish the task. The figure also indicates that the volume weighted average remeshing method and the adaptive remeshing every 10 increments are appropriate choices for this analysis.

7.2. Tip resistance (q_c) vs penetration

Typical results showing CPT tip resistance, q_c, vs penetration for several different ϕ and σ'_{vo} are shown in Figure 6. As seen in the figure, the penetration depth required to reach steady state varies from approximately 90 and 130 mm for $\phi = 32°$ ($\sigma'_{vo} = 0.05$ MPa) and 34° ($\sigma'_{vo} = 0.35$ MPa), respectively to approximately 330–350 mm for $\phi = 42°$ ($\sigma'_{vo} = 0.35$ MPa). Dense sand requires greater penetration distance to reach steady state than loose sand. The reason is that the volumetric strain near the cone is greater for loose sand, therefore the radial displacements decrease much sooner with distance for loose sand. Based on the result, we can conclude that tip resistance (q_c) in dense sand would be affected by the soil approximately 300–400 mm (8–11 cone diameters) above the cone tip. The present analysis does not allow for a conclusion regarding the zone of influence below the cone tip. Nevertheless, it is likely that this zone would be at least as large as the zone above. Using the same argument, the tip resistance would be affected by the soil approximately 100 mm (3 cone diameters) above and below the cone tip for loose sand under low initial stress.

7.3. Sleeve resistance

The typical friction resistance, f_s, at the centre of the sleeve and a distribution of resistance along its length are shown in Figure 7(a) and 7(b), respectively. The high frequency fluctuation observed in Figure 7(a) is large due to the ABAQUS algorithm, the mesh size, the contact interface, and the parameters of soil and steel. However, the average sleeve friction can still be determined, which in this case is approximately 0.029 MPa. With q_c of 2.05 MPa, the friction ratio (FR) is 1.4%. Based on Robertson and Campanella [35], soil with FR = 1.4%, q_c = 2.05 MPa, and $\sigma'_{vo} = 0.05$ MPa would be interpreted as silty sand to sandy silt and silt. Douglas and Olsen [36] will interpret the soil by the unified classification system as SM & SP, non-cohesive coarse-grained and fine-grained to non-cohesive coarse-grained.

From Figure 7(b) we note that the sleeve friction close to the cone tip is low but gradually builds to a relatively uniform value at a distance of approximately 30 mm from the bottom of the shaft (40 mm from the cone tip) for $\phi = 34°$ and $\sigma'_{vo} = 0.05$ MPa. The observation by Kiousis et al. [13] confirms this non-uniform sleeve friction distribution. They found that there was a very thin separation between soil and cone shaft interface for approximately 35 mm above the upper end of the cone tip. This finding suggests a possible need to move the sleeve location in CPT probes away from the tip if a uniform frictional distribution is desired. Further research of
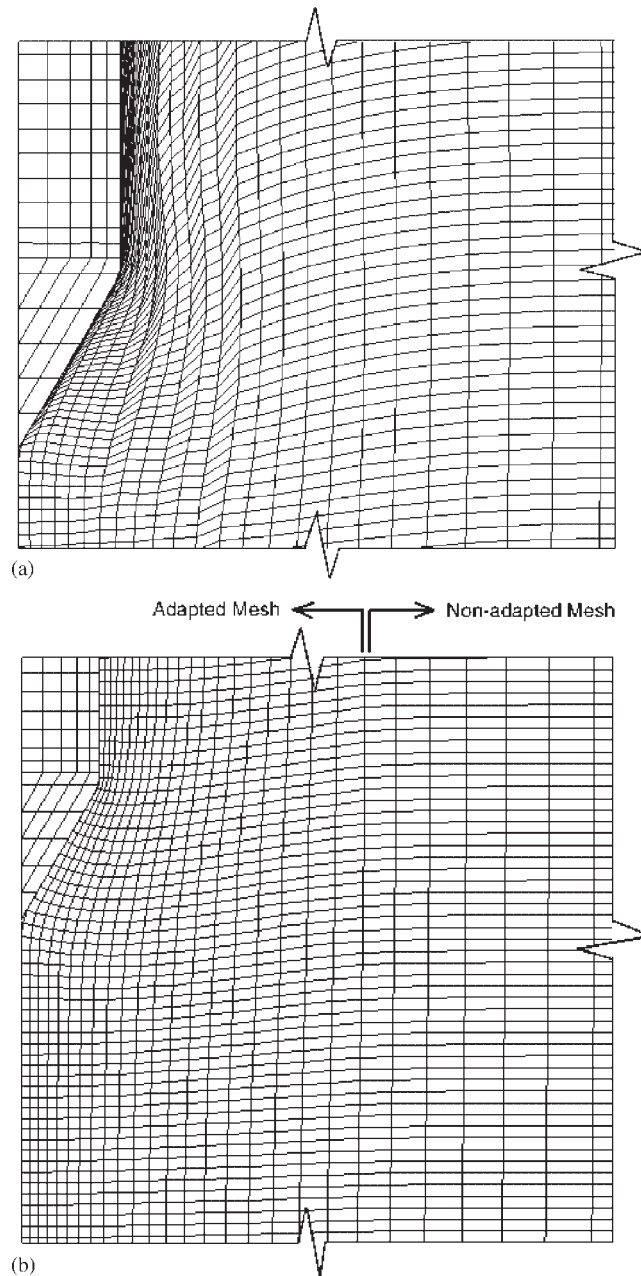
Figure 5. (a) Deformed mesh without remeshing. (b) Deformed mesh using auto-adaptive remeshing.

this sleeve distribution is certainly needed especially for different soil types and strengths. Additional research is also needed to reduce the fluctuation of friction along the sleeve in numerical modelling.
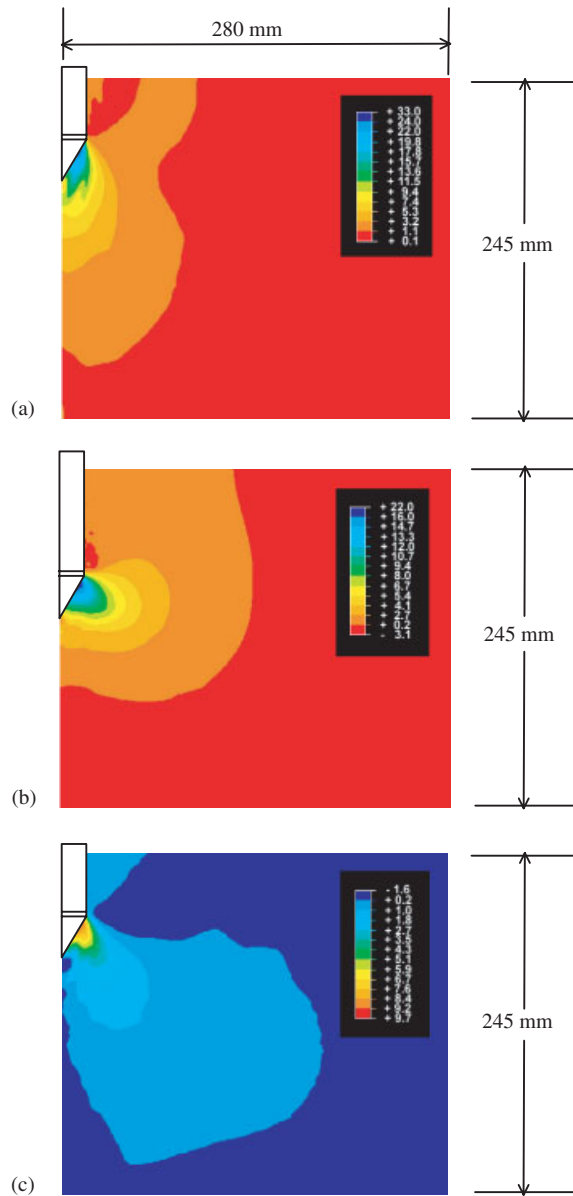
Plate 1. Typical normalized stresses around cone tip after steady state: (a) Vertical (σ'_v/σ'_{vo}), (b) Horizontal (σ'_h/σ'_{vo}), and (c) Shear (τ'/σ'_{vo}) for $\phi = 34°$ and $\sigma'_{vo} = 0.05$ MPa.
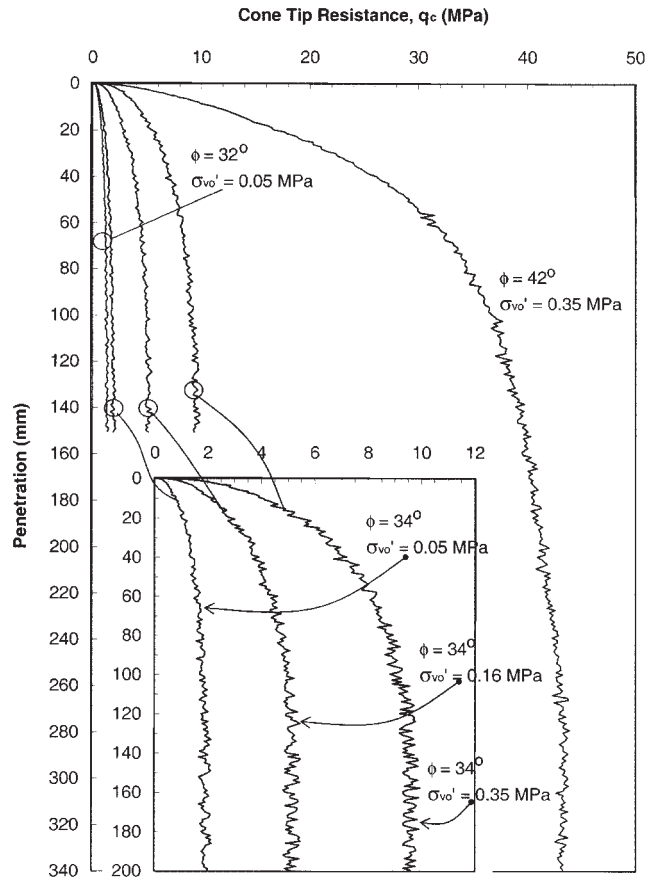
Cone Tip Resistance, q_c (MPa)

Figure 6. Tip resistance (q_c) vs penetration.

7.4. Contours of stress

Plates 1(a)–1(c) present the contours of normalized shear stress, τ/σ'_{vo}, normalized effective vertical stress, σ'_v/σ'_{vo}, and normalized effective horizontal stress, σ'_h/σ'_{vo}, after tip resistance attains a steady state. The contours show that σ'_h/σ'_{vo} and σ'_v/σ'_{vo} surrounding the cone tip increase greatly due to penetration. For example, the σ'_h/σ'_{vo} increases from an initial $\sigma'_{ho}/\sigma'_{vo}$ of 0.44 (at $\sigma'_{vo} = 0.05$ MPa) to more than 14 (more than 25 times higher) right below the cone tip. For higher initial stress (σ'_{vo}), the increase σ'_h/σ'_{vo} will be lower. While the ratio of σ'_h to σ'_v (K) is initially higher in loose sand, as estimated by $K_o = 1 - \sin\phi$ [26], it becomes higher for dense sand after penetration reaches a steady state.

Plate 1(c) also reveals an area of slightly lower horizontal stress immediately above the cone tip. The lower horizontal stress may partly explain the lower sleeve friction resistance measured on the sleeve friction elements just above the cone as shown in Figure 7(b). We can also see from Plate 1 that the vertical, horizontal, and shear stresses are higher near the upper end of the cone than near the tip. The main reason for this condition is the inherent corner geometry which
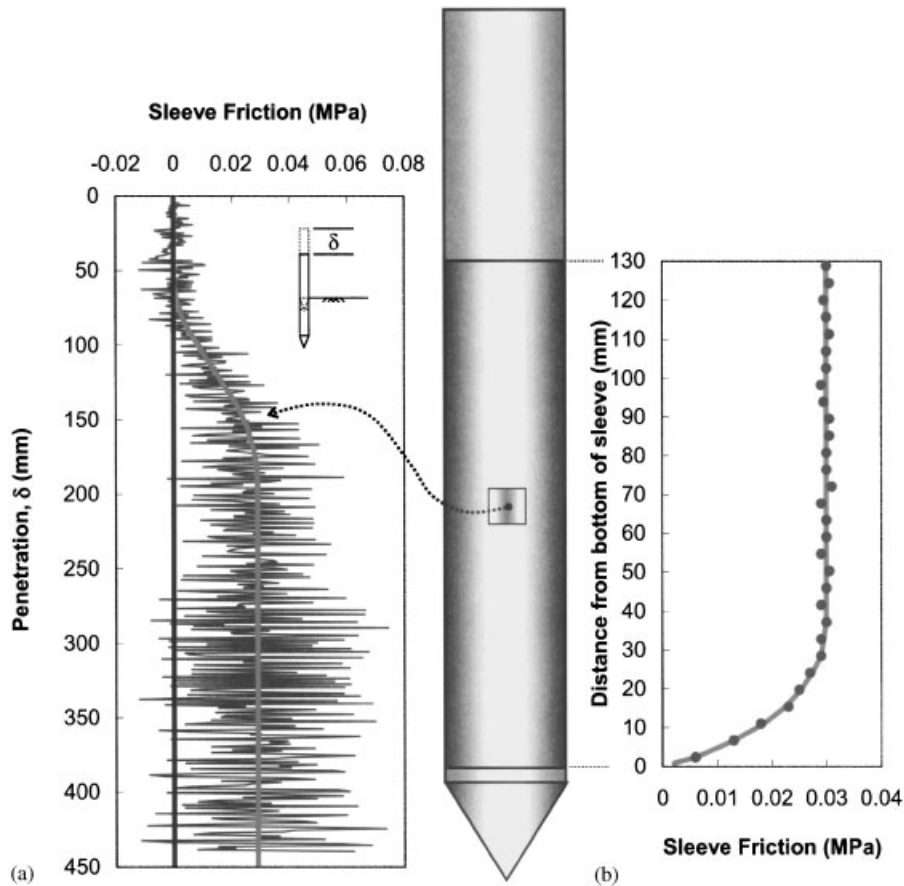
Figure 7. (a) Typical sleeve friction at center of cone sleeve during penetration. (b) Typical distribution of friction resistance along the sleeve (for $\phi = 34°$ and $\sigma'_{vo} = 0.05$ MPa).

results in stress-build-up. The frictional interface between the cone and sand most likely also contributes to the shifting of stresses to the upper end of the tip.

7.5. Cone resistance

Figure 8 shows the relationship between q_c, σ'_{vo}, and ϕ at steady state. In Figure 9, the present analysis results are compared with other methods summarized by Yu and Mitchell [37] which consist of: HH—average chamber correlation of Houlsby and Hitchman [11]; DM—bearing capacity solution of Durgunoglu and Mitchell [3–4]; LJ&C—cavity expansion solution of Collins et al. [38] combined with bearing capacity factor correlation of Ladanyi and Johnston [39]; and YH&C—cavity expansion solution of Collins et al. [38] combined with correlation of Yasafuku and Hyde [40]; G—experimental chamber test for normally consolidated Ticino sand by Ghionna [41]. The initial mean confining stress before penetration for the data in Figure 9(a)
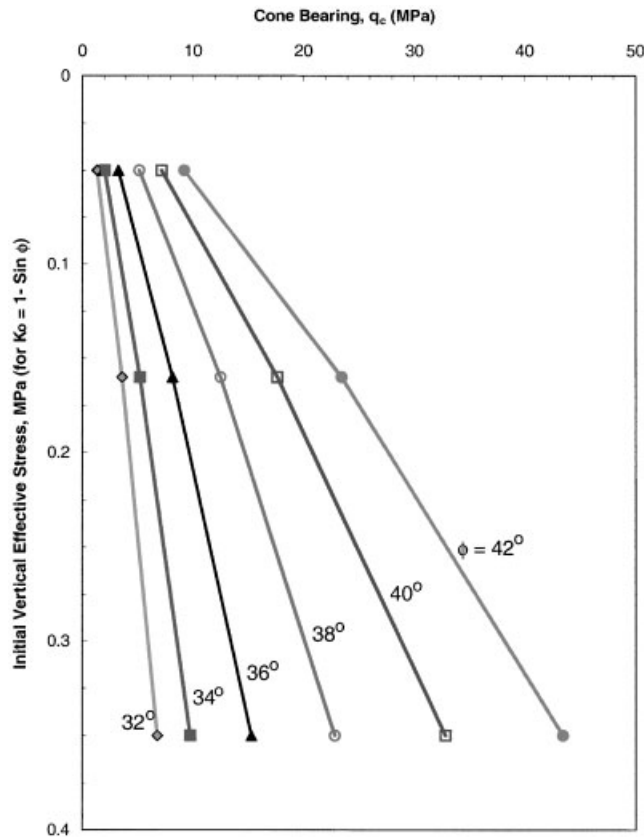
Figure 8. q_c vs σ'_{vo} relation with ϕ.

ranges from 0.037 to 0.047 MPa, while the mean initial stress in the present study ranged from 0.03 to 0.04 MPa depending on K_o. In Figure 9(b) the mean initial stress in the referenced data ranges from 0.189 to 0.237 MPa while the mean stress in the present study ranges from 0.19 to 0.23 MPa.

We can see from Figures 9(a) and 9(b) that the present analysis results compare very well with other methods, especially with the experimental chamber test results for normally consolidated Ticino sand [41]. The experimental tests using Ticino sand provide excellent comparison because Ticino sand has $\phi_{cv} = 32–34°$ [42] while quartz sand has $\phi_{cv} = 33°$ [28]. Excellent agreement with the experimental tests by Ghionna [41] can even be noticed at low initial mean stress as can be shown in Figure 9(a). The difference of the predicted angle of internal friction between the present study and other methods at low initial stress is approximately 0–2°, the exception being Houlsby and Hitchman [11]. For high initial stress ($\sigma'_{vo} = 0.35$ MPa) cases, as shown in Figure 9(b), the present analysis results also compare very well with all other methods especially with Ghionna's experimental results [41]. The difference of the predicted angles of internal friction between this present study and other methods for high initial stress, is approximately 0–3°.
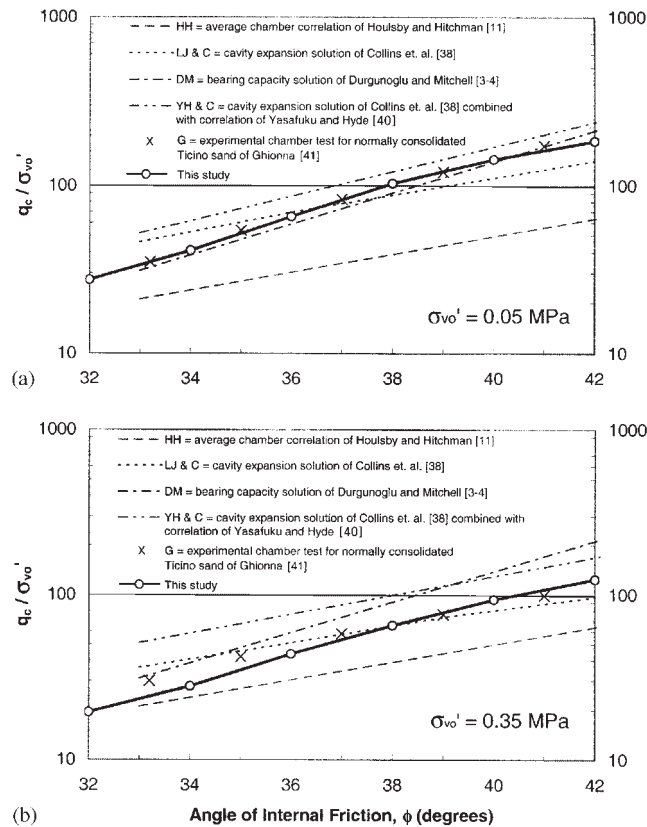
Figure 9. Comparison between FE results with previous models (After Yu and Mitchell [37]).

8. SUMMARY AND CONCLUSIONS

A study of cone penetration into normally consolidated clean sands using an auto-adaptive remeshing finite element model has been presented. The study shows that auto-adaptive remeshing maintains a high quality mesh and avoids numerical problems that would otherwise develop due to high distortion of soils surrounding the cone tip. The other significant improvements are the modelling of a frictional interface; a special boundary which prohibits soil from displacing across the axis-symmetric centre line; and the infinite elements at the periphery of the model. Sand was modeled using a non-associative Drucker–Prager constitutive model. Coulomb friction was chosen for the interface constitutive law between steel and sand. Despite the usage of simple constitutive models both for sand and interface friction, the finite element model was able to simulate cone penetration into sand with results in excellent agreement with earlier analytical and experimental studies.

The q_c-displacement curves suggest that dense sand requires greater penetration to reach steady state. In dense sand, tip resistance (q_c) is affected by the soil within a 600–800 mm (16–22 cone diameters) zone above and below the cone tip while in loose sand the zone is approximately

180–260 mm (5–7 cone diameters). The proposed chart for predicting angles of internal friction based on tip resistance (q_c) and initial stress (σ'_{vo}) is in good agreement with other methods, only differing by 0–3°. The present analysis also shows that the distribution of sleeve resistance along the cone sleeve is not uniform. It is significantly lower close to the cone tip and becomes uniform higher up along the sleeve. This finding may eventually result in a recommendation to move the location of the cone sleeve further from the cone tip.

ACKNOWLEDGEMENTS

REFERENCES

1. Meyerhof GG. The ultimate bearing capacity of wedge-shaped foundation. *Proceedings of the 5th International Conference On Soil Mechanics and Foundations* 1961; **2**:103–109.
2. Janbu N, Senneset K. Effective stress interpretation of in-situ static cone penetration tests. *Proceedings of the 1st European Symposium On Penetration Testing* 1974; **2**:181–193.
3. Durgunoglu HT, Mitchell JK. Static penetration resistance of soils: I. Analysis. *Proceedings of the Conference on In Situ Measurement of Soil Properties*, ASCE, New York, N.Y. 1975; **1**:151–171.
4. Durgunoglu HT, Mitchell JK. Static penetration resistance of soils: II. Evaluation of theory and implications for practice. *Proceedings of the Conference on In Situ Measurement of Soil Properties*, ASCE, New York, N.Y. 1975; **1**:172–189.
5. Vesic AS. Expansion of cavities in infinite soil mass. *Journal of the Soil Mechanics and Foundation Division* 1972; **98**:265–290.
6. Baligh MM. Cavity expansion in sands with curved envelopes. *Journal of the Geotechnical Engineering Division* 1976; **11**:1131–1146.
7. Salgado R, Mitchell JK, Jamiolkowski M. Cavity expansion and penetration resistance in sand. *Journal of Geotechnical and Geoenvironmental Engineering* 1997; **123**:344–354.
8. Baligh MM. The strain path methods. *Journal of the Geotechnical Engineering*, ASCE 1985; **111**:1128–1136.
9. Baldi G, Bellotti R, Ghionna V, Jamiolkowski M, Pasqualini. Cone resistance of a dry medium sand. *Proceedings of the 10th International Conference on Soil Mechanics and Foundation Engineering*, Stockholm. 1981; **2**:427–432.
10. Belloti R, Bizzi G, Ghionna V. Design, construction, and use of a calibration chamber. *Proceedings of ESOPT*, vol. **2**. Balkema, Amsterdam, The Netherlands, 1982; 439–446.
11. Houlsby GT, Hitchman R. Calibration chamber tests of a cone penetrometer in sand. *Geotechnique* 1988; **38**(1): 39–44.
12. Ghionna V, Jamiolkowski M. A critical appraisal of calibration chamber testing of sands. In *Proceedings of the 1st International Symposium On Calibration Chamber Testing* (*ISOCCT1*), Huang AB (ed.). Elsevier Applied Science: New York, N.Y. 1991; 13–39.
13. Kiousis PD, Voyiadjis GZ, Tumay MT. A large strain theory and its application in the analysis of the cone penetration mechanism. *International Journal for Numerical and Analytical Methods in Geomechanics* 1988; **12**:45–60.
14. Van Den Berg P, De Borst R, Huetink H. An Eulerean finite element model for penetration in layered soil. *International Journal for Numerical and Analytical Methods in Geomechanics* 1996; **20**(12):865–886.
15. Abu-Farsakh MY, Voyiadjis GZ, Tumay MT. Numerical analysis of the miniature Piezocone Penetration Tests (PCPT) in cohesive soils. *International Journal for Numerical and Analytical Methods in Geomechanics* 1998; **22**(10):791–818.
16. Van Den Berg, P. Analysis of soil penetration. *Ph.D. Thesis*, Delft University, Delft, The Netherlands.
17. Hamel V, Roelandt JM, Gacel JN, Schmit F. Finite element modelling of clinch forming with automatic remeshing. *Computers & Structures* 2000; **77**(2):185–200.
18. Rebelo, N, Nagtegaal JC, Taylor LM. Comparison of implicit and explicit finite element methods in the simulation of metal forming processes. In *Numerical Methods in Industrial Forming Processes*, Chenot, Wood, Zienkiewicz (eds). 1992; 99–108.
19. Sun JS, Lee KH, Lee HP. Comparison of implicit and explicit finite element methods for dynamic problems. *Journal of Materials Processing Technology* 2000; **105**(1):110–118.
20. Hibbit, Karlsson & Sorensen (UK) Ltd and Genesis Centre. Applications of implicit and explicit finite element techniques to metal forming. *Journal of Materials Processing Technology* 1994; **45**:649–656.
21. Hibbit, Karlsson & Sorensen, Inc. *ABAQUS/Explicit User's Manual*. Version. 5.8., 1998.

22. Zienkiewicz OC, Zhu JZ. Adaptivity and mesh generation. *International Journal for Numerical Methods in Engineering* 1991; **32**:783–810.
23. Askes H, Sluys LJ. Remeshing strategies for adaptive ALE analysis of strain localization. *European Journal of Mechanics and Solids* 2000; **19**: 447–467.
24. Hyun S, Lindgren L. Smoothing and adaptive remeshing schemes for graded element. *Communications in Numerical Methods in Engineering* 2001; **17**: 1–17.
25. Van Leer B. Towards the ultimate conservative difference scheme III. Upstream-centered finite difference schemes for ideal compressible flow. *Journal of Computational Physics* 1977; **23**:263–275.
26. Van Leer B. Towards the ultimate conservative difference scheme IV. A new approach to numerical convection. *Journal of Computational Physics* 1977; **23**:276–299.
27. Jaky J. Pressure in Silos. *Proceedings of the 2nd International Conference On Soil Mechanics and Foundation Engineering*, Rotterdam, 1948; **1**:103–107.
28. Bolton MD. The strength and dilatancy of sands. *Geotechnique* 1986; **36**(1):65–78.
29. Drucker and Prager. Soil mechanics and plastic analysis or limit design. *Quarterly of Applied Mathematics* 1952; **10**(2):157–165.
30. Chen WF. *Constitutive Equations for Engineering Materials*. Wiley-Interscience Publication, John Wiley & Sons: New York, 1982.
31. Duncan JM, Chang CY. Nonlinear analysis of stress and strain in soils. *Journal of the Soil Mechanics and Foundation Division*, ASCE 1970; **5**:1629–1653.
32. Byrne PM, Cheung H, Yan L. Soil parameters for deformation analysis of sand masses. *Canadian Geotechnical Journal* 1987; **3**(3):366–376.
33. Duncan JM, Byrne P, Wong KS, Mabry P. Strength, stress-strain and bulk modulus parameters for finite element analyses of stresses and movements in soil masses. *Report No. UCB/GT/80-01*, Department of Civil Engineering, The University of California, Berkeley, 1980.
34. Boscardin MD, Selig ET, Lin R, Yang G. Hyperbolic parameters for compacted soils. *Journal of the Geotechnical Engineering* ASCE 1990; **116(1)**:88–104.
35. Robertson PK, Campanella RG. Interpretation of cone penetration test – part I (Sand). *Canadian Geotechnical Journal* 1983; **20**(4):718–733.
36. Douglas BJ, Olsen RS. Soil classification using electric cone penetrometer. *Symposium on Cone Penetration Testing and Experience*, Geotechnical Engineering Division, ASCE. St. Louis. Session No. 24, October 1981.
37. Yu HS, Mitchell JK. Analysis of cone resistance: Review of methods. *Journal of Geotechnical and Geoenvironmental Engineering* 1998; **124**(2):140–149.
38. Collins IF, Pender MJ, Wang Y. Cavity expansion in sands under drained loading conditions. *International Journal for Numerical and Analytical Methods in Geomechanics* 1992; **16**(1):3–23.
39. Ladanyi B, Johnston GH. Behavior of circular footings and plate anchors embedded in permafrost. *Canadian Geotechnical Journal* 1974; **11**:531–553.
40. Yasafuku N, Hyde AFL. Pile end bearing capacity in crushable sands. *Geotechnique* 1995; **45**(4):663–676.
41. Ghionna, V. Influence of chamber size and boundary conditions on the measured cone resistance. *Seminar, Cone Penetration Testing in the Laboratory*, University of Southampton, Southampton, U.K. 1984.
42. Manassero, M. Stress–strain relationships from drained self-boring pressuremeter tests in sands. *Geotechnique* 1989; **39**(2): 293–307.